

Single-molecule spectroscopy reveals chaperone-mediated expansion of substrate protein

Ruth Kellner^a, Hagen Hofmann^{a,1}, Alessandro Barducci^b, Bengt Wunderlich^a, Daniel Nettels^a, and Benjamin Schuler^{a,2}

^aDepartment of Biochemistry, University of Zurich, CH-8057 Zurich, Switzerland; and ^bLaboratoire de Biophysique Statistique, École Polytechnique Fédérale de Lausanne, CH-1015 Lausanne, Switzerland

Edited by Arthur L. Horwich, Yale University School of Medicine, New Haven, CT, and approved August 5, 2014 (received for review April 18, 2014)

Molecular chaperones are an essential part of the machinery that avoids protein aggregation and misfolding in vivo. However, understanding the molecular basis of how chaperones prevent such undesirable interactions requires the conformational changes within substrate proteins to be probed during chaperone action. Here we use single-molecule fluorescence spectroscopy to investigate how the DnaJ–DnaK chaperone system alters the conformational distribution of the denatured substrate protein rhodanese. We find that in a first step the ATP-independent binding of DnaJ to denatured rhodanese results in a compact denatured ensemble of the substrate protein. The following ATP-dependent binding of multiple DnaK molecules, however, leads to a surprisingly large expansion of denatured rhodanese. Molecular simulations indicate that hard-core repulsion between the multiple DnaK molecules provides the underlying mechanism for disrupting even strong interactions within the substrate protein and preparing it for processing by downstream chaperone systems.

Hsp70 | Hsp40 | Förster resonance energy transfer | protein folding | FRET

Maintaining protein homeostasis in vivo requires a tight regulation of protein folding to prevent misfolding and aggregation. Molecular chaperones have evolved as an essential part of the cellular machinery that facilitates such processes in the complex and crowded environment of a living cell (1, 2). To assist protein folding, many chaperones proceed through complex conformational cycles in an ATP-dependent manner (3–5). For several chaperone systems, these cycles have been investigated in great detail by experiment and simulation (6–8). A remarkable example are the heat shock protein (Hsp) 70 chaperones, which are essential in prokaryotes and eukaryotes and are involved in co-translational folding, refolding of misfolded and aggregated proteins, protein translocation, and protein degradation (9). The Hsp70 chaperone DnaK from *Escherichia coli* together with its co-chaperone DnaJ and the nucleotide exchange factor GrpE form an ATP-driven catalytic reaction cycle (7) (Fig. 1A). Many denatured or misfolded substrate proteins are first captured by DnaJ and subsequently transferred to the DnaK–ATP complex, with DnaK in an open conformation. Substrate and DnaJ synergistically trigger DnaK's ATPase activity, which leads to locking of the substrate in the DnaK–ADP complex, with DnaK in the closed conformation. Driven by the following GrpE-catalyzed ADP–ATP exchange, the DnaK–substrate complex dissociates (10). Since this ATP-driven cycle can even solubilize protein aggregates (11, 12), substantial forces must be transduced to the substrate protein (13–15). However, as for other chaperone systems (16), surprisingly little is known about how these forces and the resulting constraints of the underlying free energy surfaces affect the conformations of the denatured or misfolded substrate proteins. To better understand this important link between chaperone action and function, we probed the conformation of a substrate protein along the different stages of the chaperone cycle of DnaK with single-molecule Förster resonance energy transfer (smFRET), correlation spectroscopy, and microfluidic mixing.

Results and Discussion

Single-Molecule Spectroscopy of Substrate–Chaperone Complexes. A key strength of smFRET is to resolve subpopulations of molecules by their intramolecular distances, which is especially advantageous for investigating the conformational heterogeneity of denatured proteins and chaperone–substrate complexes (17, 18). The combination with microfluidic mixing devices enables the time-resolved observation of transient aggregation-prone species, such as denatured chaperone substrates at near-physiological conditions (19, 20). To obtain detailed information about the substrate conformation for each step in the Hsp70 chaperone cycle, we mapped several segments within the classic chaperone substrate protein rhodanese. Several protein variants were designed to report on different aspects of the structure of rhodanese (Fig. 1B): the conformation of the N-terminal domain ($\Delta 58$: E77C/K135C), the C-terminal domain ($\Delta 49$: K236C/E285C), the linker connecting both domains ($\Delta 39$: K135C/K174C), and the relative arrangement of the two domains, with the fluorophores attached close to the domain interface ($\Delta 117$: D102C/D219C) or on opposite sides of the domains ($\Delta 159$: E77C/K236C). Alexa Fluor 488 as a FRET donor and Alexa Fluor 594 as an acceptor were attached to each variant to obtain information on the distance between the corresponding amino acid residues. Fig. 1C shows transfer efficiency histograms for the five variants of rhodanese, determined from fluorescence bursts of individual molecules freely diffusing through the observation volume of the confocal instrument. The folded proteins (Fig. 1C, gray histograms) exhibit characteristic transfer efficiency distributions with averages close to the values expected from the crystal structure of rhodanese.

Significance

Molecular chaperones are a group of proteins that are essential for avoiding the aggregation of other proteins in the crowded cellular environment. Chaperones function by interacting with these substrate proteins in different ways. However, it has remained a challenge to measure the changes that occur in the substrate proteins and understand how these changes prevent misfolding or aggregation. Here we investigate a chaperone system that keeps the substrate protein denatured by clamping the polypeptide chain. We observe an expansion of the substrate protein chain up to 30-fold in volume owing to steric repulsion between multiple copies of the chaperone bound to a single substrate protein. In this way, unwanted interactions within or between substrate proteins can be prevented.

Author contributions: H.H. and B.S. designed research; R.K., H.H., and A.B. performed research; H.H., B.W., and D.N. contributed new reagents/analytic tools; R.K., A.B., and D.N. analyzed data; and R.K., H.H., A.B., and B.S. wrote the paper.

The authors declare no conflict of interest.

This article is a PNAS Direct Submission.

¹Present address: Department of Structural Biology, Weizmann Institute of Science, Rehovot 76100, Israel.

²To whom correspondence should be addressed. Email: schuler@bioc.uzh.ch.

This article contains supporting information online at www.pnas.org/lookup/suppl/doi:10.1073/pnas.1407086111/-DCSupplemental.

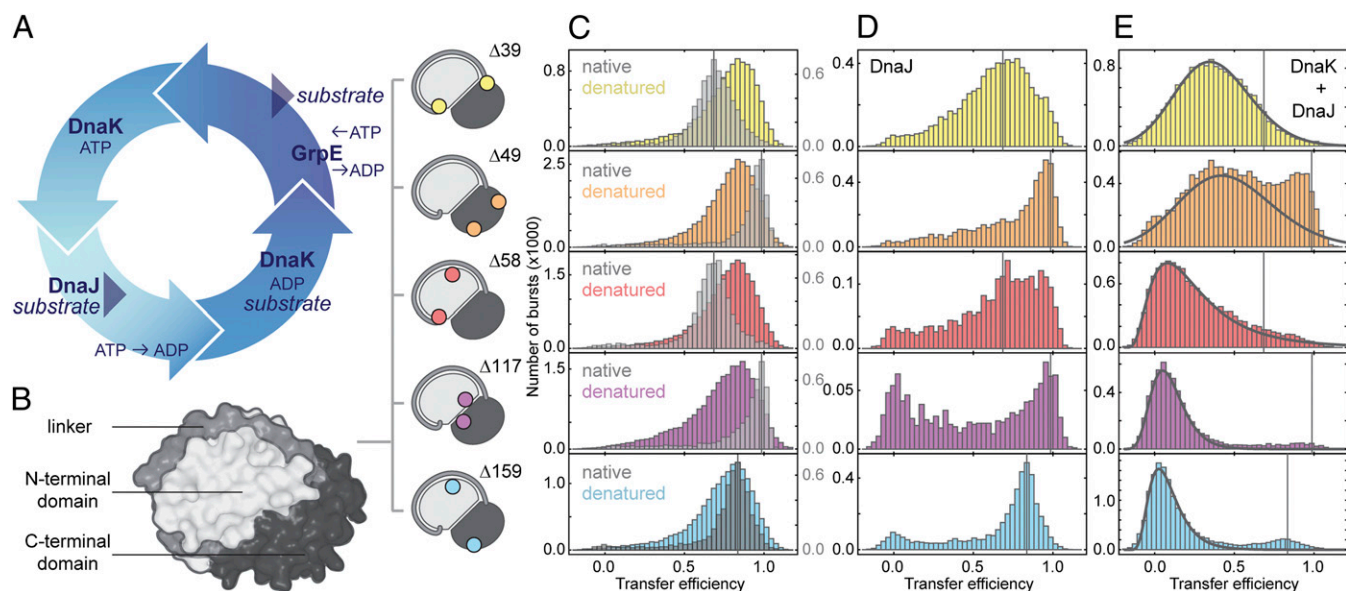


Fig. 1. DnaK expands the denatured substrate protein. (A) Illustration of the DnaK–ATPase cycle. (B) Surface representation of rhodanese (PDB ID code 1RH5) with the subdomains indicated in different gray levels and the label positions of fluorescent dyes for single-molecule FRET measurements shown schematically. (C) FRET efficiency histograms of native rhodanese (gray) and denatured rhodanese under native conditions transiently populated in the microfluidic mixer (colored, measured 125 ms after dilution of rhodanese into native conditions). (D) FRET efficiency histograms of DnaJ–rhodanese complexes (0.5 μ M DnaJ). (E) FRET efficiency histograms of DnaK–rhodanese complexes (0.5 μ M DnaJ, 10 μ M DnaK, and 1 mM ATP; DnaK and DnaJ were added simultaneously to rhodanese). Black lines indicate the DnaK–rhodanese complex population resulting from a fit that takes into account the residual population of refolded and DnaJ-bound rhodanese. The vertical lines in C–E indicate the positions of the FRET efficiency peaks of the native population of the respective rhodanese variants. The small populations at zero transfer efficiency in D (note the axis scaling and the small amplitudes of this population compared with E) originate from incomplete elimination of molecules with inactive acceptor fluorophores by pulsed interleaved excitation.

Here, however, our focus is on the conformation of denatured rhodanese (Fig. 1C, colored histograms). As a reference state in the absence of chaperones and denaturant, we thus transiently populate denatured rhodanese in a microfluidic mixing device by rapid dilution of guanidinium chloride (GdmCl) (19, 21–23). In contrast to native rhodanese, all denatured rhodanese variants exhibit a similar and high transfer efficiency of ~ 0.8 , which suggests the presence of a compact denatured state ensemble under these conditions (24). Denatured rhodanese is highly prone to aggregation during refolding (25), but at the extremely low protein concentrations used here (50 pM) aggregation does not occur, and all variants fold to the native state spontaneously on a timescale of minutes, even in the absence of chaperones (19) (Fig. S1C).

When GdmCl-denatured rhodanese is diluted into buffer in the presence of DnaJ in the physiological concentration range (0.5 μ M) (26), the resulting transfer efficiency histograms (Fig. 1D) are remarkably different from those of folded and denatured rhodanese (Fig. 1C). Very broad transfer efficiency distributions are obtained for all variants of rhodanese in complex with DnaJ (Fig. 1D), suggestive of a heterogeneous distribution of conformations. Only a fraction of rhodanese molecules ($\sim 10\%$) fold to their native structure (Fig. 1D, Fig. S1, and Table S1), as indicated by the subpopulations at the same transfer efficiency as the folded state. Given the rate constant of $\sim 3 \times 10^{-3} \text{ s}^{-1}$ for the spontaneous refolding of rhodanese in the absence of chaperones (Fig. S1 and Table S1) under these conditions (19, 27), the association rate constant of DnaJ to denatured rhodanese can be estimated to be $\sim 4 \times 10^4 \text{ M}^{-1} \text{ s}^{-1}$ (Fig. S1 and Table S1). In addition to the broad transfer efficiency distributions, DnaJ binding of denatured rhodanese results in a loss in brightness of the attached fluorophores (Table S2), indicative of quenching by solvent-exposed aromatic amino acid residues in a relatively compact denatured state of rhodanese (28). Time-resolved single-molecule anisotropy experiments reveal only a moderately increased fluorescence anisotropy of the attached fluorophores in

the DnaJ–rhodanese complex (Table S2); a dominant influence of orientational heterogeneity on the transfer efficiency histograms (20) is thus unlikely. The quenching of the attached fluorophores together with the broad transfer efficiency distributions thus suggest that DnaJ blocks rhodanese refolding by holding it in a heterogeneous ensemble of nonnative conformations that are substantially different from those of denatured rhodanese in the absence of chaperones (Fig. 1C, gray histograms, and D).

To obtain independent information on the size of the rhodanese–DnaJ complexes, we used two-focus fluorescence correlation spectroscopy (2f-FCS), where the cross-correlation between the fluorescence intensities from two partially overlapping foci is used to determine the translational diffusion time and the corresponding Stokes radius, R_S , of the complex (29). For both folded and denatured rhodanese in the absence of chaperones, we observe $R_S = 2.6 \pm 0.1 \text{ nm}$, which confirms the compactness of denatured rhodanese indicated by the transfer efficiencies (Fig. 1C). Binding of rhodanese to DnaJ at 0.5 μ M results in an increase in R_S to $3.1 \pm 0.2 \text{ nm}$. Even if we assume a very compact configuration of this complex and the contribution of a small fraction of refolded rhodanese (Fig. S1E), this value of R_S is incompatible with more than one DnaJ dimer (30) bound per rhodanese molecule (Table S3). Nevertheless, the rhodanese–DnaJ-bound state is very stable and persists for more than 24 h under our experimental conditions (Fig. S2). In summary, our results suggest that DnaJ arrests rhodanese in a compact, but denatured and folding-incompetent, state. The next step in the chaperone cycle is the interaction of this complex with DnaK.

Expansion of Rhodanese by DnaK. The addition of 10 μ M DnaK and 1 mM ATP to preformed rhodanese–DnaJ complexes leads to surprisingly large changes in the transfer efficiency histograms (Fig. 1E). A pronounced shift of the distributions to lower transfer efficiencies is observed, indicating that DnaK binding leads to the formation of highly expanded conformations of

rhodanese. At the same time, the brightness of the molecules increases (Table S2), as expected from the increased distances between the FRET dyes and aromatic amino acids in a more expanded chain (28). The resulting conformational ensembles of rhodanese, which are even more expanded than rhodanese unfolded in 6 M GdmCl (Fig. S1G) (18, 31), are observed independent of whether DnaK and ATP are added to preformed DnaJ complexes or whether DnaJ, DnaK, and ATP are added at the same time (Fig. S3A). Since the collapse of unfolded proteins upon transfer into non-denaturing conditions occurs on time-scales in the range of ~ 100 ns to ~ 100 μ s (32–36), much faster than the association rate of DnaJ and DnaK to rhodanese (~ 1 min $^{-1}$, discussed below), the chaperones bind rhodanese in its compact denatured state (Fig. 1C).

The formation of rhodanese–DnaK complexes is strictly dependent on the presence of DnaJ and ATP. Neither the nonhydrolyzable ATP analog ATP γ S nor ADP can trigger the expansion of rhodanese (Fig. S3C), suggesting that the ATP-bound conformation of DnaK is crucial for binding of protein substrates such as rhodanese. In the absence of nucleotide, no DnaK-driven expansion of rhodanese was observed even after several hours (Fig. S3B). With an excess of ATP (1 mM in Fig. 1E), however, the DnaK-bound complex remains stable for hours. The expansion of denatured rhodanese also depends on the relative concentrations of DnaJ and DnaK (Fig. S3D–F). The greatest substrate expansion by DnaK is reached in the presence of ~ 0.5 μ M DnaJ and 10 μ M DnaK (Fig. S3E), which is in the physiological concentration range (26) and was thus used as the DnaJ and DnaK concentrations in the present study. This result suggests that the substoichiometric amounts of DnaJ compared with DnaK observed *in vivo* are optimized in order that DnaJ keeps substrate proteins denatured but does not saturate the polypeptide, which would interfere with DnaK binding, because both chaperones recognize similar amino acid patterns in their substrates (37). Correspondingly, high concentrations of DnaJ (10 μ M) inhibit the DnaK-mediated expansion of rhodanese (Fig. S3D–F) by occupying binding sites on rhodanese, as indicated by the larger complex size of DnaJ–rhodanese at 10 μ M DnaJ (R_S determined with 2f-FCS: 5.4 ± 0.2 nm) compared with the complex at 0.5 μ M DnaJ. Although the substrate-like binding of DnaJ to DnaK (38, 39) may contribute to a reduction of the DnaK concentration available for rhodanese binding, the affinity between the chaperones is not high enough (38) to explain the absence of the expansion of rhodanese at high DnaJ concentrations. Notably, denatured rhodanese cannot be expanded by DnaK and ATP in the absence of DnaJ (Fig. S3C), in agreement with the previously suggested sequential action of DnaJ and DnaK (13). The reason underlying the lack of DnaK–substrate binding in the absence of DnaJ was identified in previous studies that showed that a functionally impaired J domain of DnaJ is not able to couple DnaK–substrate binding and ATP hydrolysis for efficient DnaK–substrate complex formation (38, 39).

In contrast to the compact denatured state of rhodanese alone (Fig. 1C, colored histograms), the mean transfer efficiency of the five rhodanese variants bound to DnaK shows a clear decrease in efficiency with increasing sequence separation between the dyes (Fig. 2C, circles). In terms of intramolecular distances, this observation translates into a pronounced increase of the interdyne distance with increasing sequence separation. This behavior is expected for rather uniformly expanded denatured proteins (40, 41) and indicates that persistent tertiary structure is absent in DnaK-bound denatured rhodanese. In comparison with denatured rhodanese in the absence of chaperones (Fig. 1C, colored histograms), the transfer efficiency distributions obtained in complex with DnaK and ATP are significantly broadened. Time-resolved fluorescence anisotropy measurements do not reveal a pronounced lack of rotational averaging of the attached fluorophores (Table S2); the broad transfer efficiency distributions are thus most likely

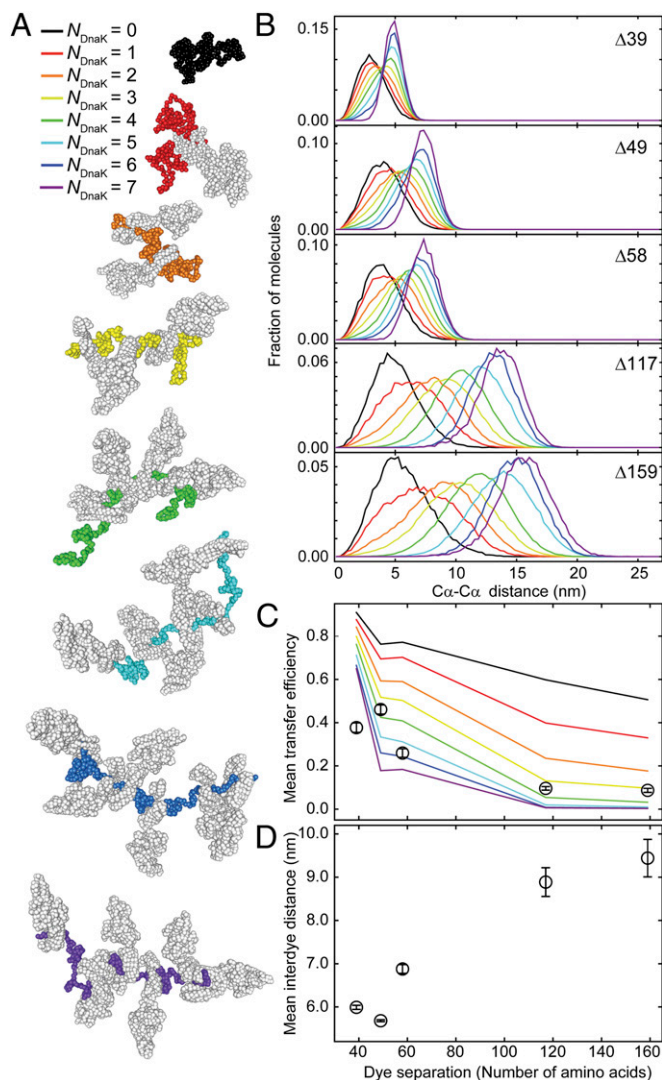


Fig. 2. Substrate expansion can be explained by excluded volume effects from binding of several DnaK molecules per substrate molecule. (A) Representative structures from molecular dynamics (MD) simulations of rhodanese bound by a varying number of DnaK molecules (N_{DnaK}) to all combinations of possible DnaK binding sites in the rhodanese sequence predicted by LIMBO (44). The color code from black to purple indicates the number of DnaK molecules (depicted in gray) bound per rhodanese (color code as indicated). (B) Interdyne distance distributions from MD simulations for the dye positions of the different rhodanese variants used in the smFRET experiments (Fig. 1) for different N_{DnaK} bound (colors as in A). (C) Comparison of the mean transfer efficiencies calculated from the distance distributions in the MD simulations in B as a function of N_{DnaK} (colored lines) and mean transfer efficiencies from single-molecule data (Fig. 1E, black circles). Error bars indicate the uncertainty due to variability in instrument calibration. (D) Mean interdyne distances from the FRET efficiency histograms (Fig. 1E) as a function of the sequence separation of the labeling positions. Mean transfer efficiencies from experimental data were converted to mean interdyne distances assuming Gaussian distributions with the shapes of the simulated distributions for $N_{DnaK} = 6$ and adjustable mean. Error bars indicate the variation of the average interdyne distance upon variation of the width of the Gaussian distribution for different N_{DnaK} .

to originate from a heterogeneous ensemble of very expanded rhodanese conformations in complex with DnaK that interconvert slowly compared with the millisecond observation time (42).

Simulations Provide the Molecular Picture. To obtain a more detailed picture of the underlying structural ensembles, we performed

molecular simulations of the DnaK–rhodanese complexes. Owing to the complexity of the system, we used a coarse-grained model (43) where denatured rhodanese is represented as a disordered α chain with weak intramolecular interactions. A structure-based model of DnaK is then bound to rhodanese in one to seven copies at positions corresponding to DnaK binding sites identified using the predictor of van Durme et al. (44) (Fig. S4). With increasing numbers of DnaK molecules bound to denatured rhodanese, the simulations clearly show an increasing expansion of the complex (Fig. 2). If we compare the mean transfer efficiencies from the smFRET experiments (Fig. 1E) with the corresponding values calculated from the different simulated ensembles (Fig. 2C), the best overall agreement is observed in a range of four to seven DnaK molecules bound to rhodanese. The lowest individual mean-square deviation is obtained for six DnaK molecules, but a distribution of stoichiometries in this range is likely to contribute to the width of the smFRET efficiency distributions. By combining the experimental transfer efficiencies with the shape of the distance distributions obtained from the simulations (Fig. 2B), we estimate the average radius of gyration of the rhodanese–DnaK complexes to be $\sim 7.2 \pm 0.3$ nm (Table S4).

We can again test the molecular dimensions independently with 2f-FCS, which allows the size of the complex to be quantified in terms of the R_S from its translational diffusivity. We obtain $R_S = 9.2 \pm 0.2$ nm for the rhodanese–DnaK complex, about a factor of three greater than the value for rhodanese bound to DnaJ, corroborating the strong DnaK-mediated expansion of the denatured protein. This value of R_S agrees well with the Stokes radii calculated from the simulations for five to six DnaK molecules bound to rhodanese (Table S4), in agreement with the analysis of the FRET measurements. Both the experiments and the simulations thus support the picture of a substrate protein whose chain is almost saturated with DnaK. The volume exclusion between the bulky DnaK molecules underlies the pronounced substrate protein expansion we observe and results in an increase of the chain volume by a factor of ~ 30 – 40 . DnaK thus strongly shifts the conformation of the substrate protein toward a fully unfolded state where intramolecular interactions are expected to be minimized.

Dynamics of Complex Formation from Microfluidic Mixing. In contrast to DnaJ, the action of DnaK on the substrate protein requires continuous binding and release driven by ATP hydrolysis (45). To quantify the dynamics underlying this nonequilibrium process, we use a combination of manual and microfluidic mixing experiments, which allows us to monitor the process from milliseconds to hours. For measurements in the microfluidic device (19, 21, 23), preformed rhodanese–DnaJ complexes and ATP entering from the two side channels are rapidly mixed with DnaK in the main channel (Fig. 3A). Rapid mixing is achieved by lateral diffusion of the components in the narrow mixing neck, and transfer efficiency histograms at different times after mixing are obtained by placing the confocal volume at different positions in the following observation channel. As expected, the expanded rhodanese–DnaK population at low transfer efficiencies increases after mixing (Fig. 3B), whereas the rhodanese–DnaJ population decreases. A global fit yields a rate constant of $k = 0.028$ s $^{-1}$ (Fig. 3C). This result is in accord with previously reported values for the conformational transition of DnaK between the open and the closed conformation triggered by DnaJ (0.04 s $^{-1}$) (46), suggesting that the conformational switch in DnaK induced by substrate binding concurs with the conformational shift in the substrate ensemble.

If the expansion of denatured rhodanese depends on the continuous hydrolysis of ATP by DnaK, we expect the system to relax back to its thermodynamic equilibrium when the ATP is consumed (Fig. 4D and Fig. S5A). Indeed, under conditions of limiting ATP concentrations (Fig. 4B–D), the extended conformation of rhodanese disappears with a rate constant of $(2.5 \pm 0.4) \cdot 10^{-3}$ s $^{-1}$

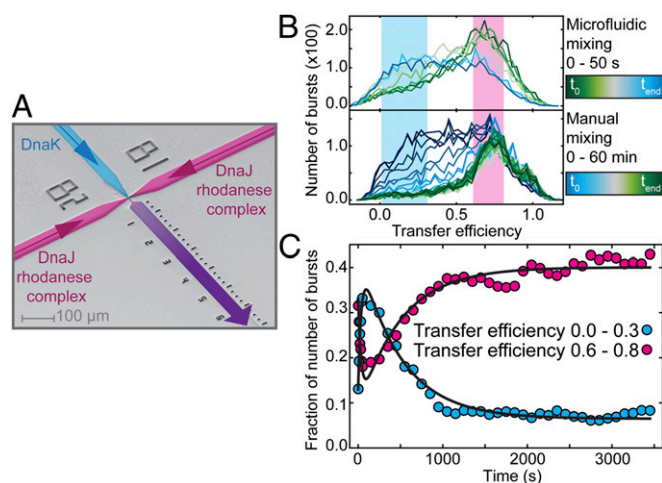


Fig. 3. Dynamics of association and dissociation of DnaK to DnaJ–rhodanese complexes. (A) Electron micrograph of the microfluidic mixing device. DnaK enters from the central channel (blue), and preformed DnaJ–rhodanese ($\Delta 39$) complexes and ATP enter from the side channels (magenta). Rapid mixing is achieved in the narrow mixing neck, and data are recorded with a confocal setup for 30 min at different positions in the observation channel (purple). FRET efficiency histograms were obtained at different times up to 50 s after mixing in the microfluidic mixing device (B, Upper) and up to 1 h after manual mixing (B, Lower). The starting concentrations were the same in both cases: 0.5 μ M DnaJ, 10 μ M DnaK, and 20 μ M ATP. FRET efficiency histograms from manual mixing measurements were constructed by moving window analysis (19) using 5-min intervals starting every 100 s. To quantify the kinetics of DnaK– and DnaJ–rhodanese complex formation over time, the fractions of bursts with transfer efficiencies ranging from 0.0 to 0.3 (blue) and from 0.6 to 0.8 (magenta) determined for each histogram are represented (C). The data were fitted globally to double exponential functions with shared rate constants for expansion and release (black lines).

(Table S1). This rate is in a similar range as previously determined off-rates for substrates from ADP-bound DnaK (38, 47, 48). After reaching equilibrium, the transfer efficiency histograms are indistinguishable from those of the DnaJ–rhodanese complex, suggesting complete dissociation of DnaK (compare Fig. 4B, final histogram, and Fig. 1D). Interestingly, within experimental error, the dissociation rate constants are identical for all rhodanese variants (Fig. 4C and Table S1). This observation suggests that the dissociation rates of DnaK are rather independent of the position on the rhodanese chain and lack binding cooperativity, also confirmed by the independence of the dissociation rate of the DnaK concentration (Fig. S6), which justifies using only excluded volume interactions between DnaK molecules in the simulations. When the dissociation of DnaK is observed with 2f-FCS, a decrease of the R_S with a rate constant of $(1.7 \pm 0.4) \cdot 10^{-3}$ s $^{-1}$ is observed (Fig. 4A, white circles), in agreement with the decay of the expanded conformation observed in the smFRET experiments (Fig. 4B and C). After completion of the dissociation reaction, the R_S of the rhodanese–DnaJ complex is recovered, supporting our conclusion that DnaK dissociates completely once all ATP is consumed (Fig. 4A). Our observation that rhodanese does not remain stably bound to DnaK at limiting ATP concentrations contrasts with studies on other substrates (e.g., luciferase or peptides) (49, 50), indicating that the stability of the complex with DnaK depends on the substrate protein or peptide (51). We note, however, that the dependence of the expansion of rhodanese on the availability of ATP is in agreement with a recent theoretical study suggesting that the effective affinity of DnaK under nonequilibrium conditions can greatly exceed the one observed for ADP-bound DnaK (52). Whether DnaJ remains bound during the DnaK-driven expansion or rebinds after DnaK release is currently unclear (but this aspect has no bearing on our conclusions).

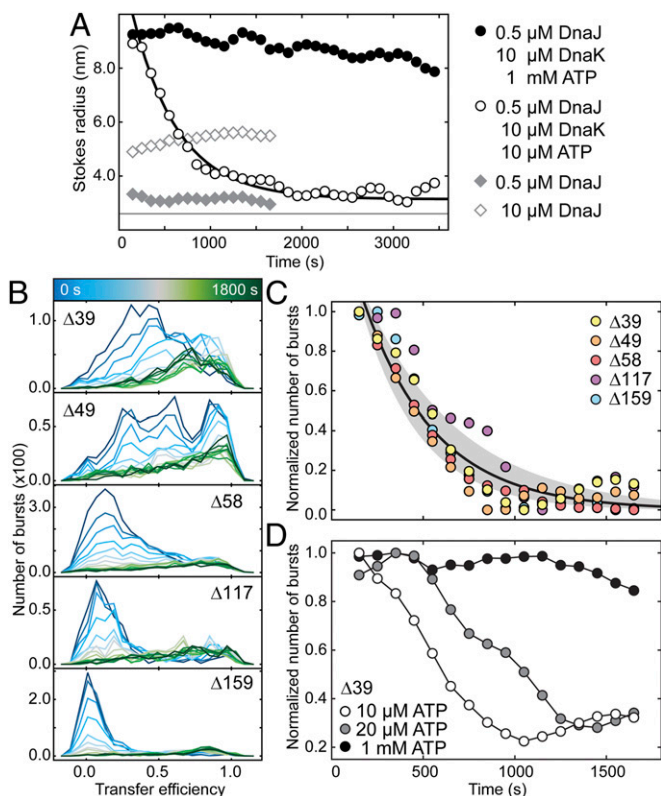


Fig. 4. DnaK release kinetics are independent of the binding site on rhodanese. (A) Stokes radii of rhodanese (K174C Alexa 488) obtained from 2f-FCS measurements as a function of time after dilution of denatured rhodanese into native buffer in the presence of 0.5 μM DnaJ (gray diamonds); 10 μM DnaJ (white diamonds), 10 μM DnaK, 0.5 μM DnaJ, and 1 mM ATP (black circles); or 10 μM DnaK, 0.5 μM DnaJ, and 10 μM ATP (white circles). For comparison, the R_s of native rhodanese is indicated as a horizontal line. The black line is a single exponential fit. (B) Time-resolved FRET efficiency histograms for the five rhodanese variants after manual dilution of denatured rhodanese into native buffer in the presence of 10 μM DnaK, 0.5 μM DnaJ, and 10 μM ATP. After formation of the DnaK–rhodanese complexes during the dead time of manual mixing, we observe complex dissociation. (C) Decay of the DnaK–rhodanese complex population from the single-molecule FRET measurements shown in B represented by the change of the total number of bursts observed in each time interval, which decreases owing to the brightness difference between rhodanese with and without DnaK bound (Fig. 1 D and E and Table S2). All decays are well described with a single rate constant (black line, with confidence interval). (D) Dissociation of the DnaK–rhodanese complexes (variant Δ39) formed at 10 μM DnaK and 0.5 μM DnaJ were measured for different starting concentrations of ATP: 1 mM ATP (black), 20 μM ATP (gray), and 10 μM ATP (white).

Closing the Cycle. The third component acting together with DnaJ and DnaK has not been considered so far: the nucleotide exchange factor GrpE (53). GrpE catalyzes the exchange of ADP with ATP in DnaK (54) and thus accelerates the nonequilibrium association/dissociation cycle of DnaK with the substrate protein (47, 55). As a result, the addition of GrpE to the rhodanese–DnaK complexes leads to a faster disappearance of the expanded rhodanese population (Fig. S5 C and D), reflecting the accelerated ATP hydrolysis by DnaK in the presence of GrpE and confirming the functionality of the entire DnaK/DnaJ/GrpE chaperone system used in our single-molecule experiments. The degree of rhodanese expansion, however, is not reduced by GrpE, indicating that the more rapid ATP turnover does not alter the average number of DnaK molecules bound per rhodanese so long as sufficient ATP is still available (Fig. S5B). As for the uncatalyzed dissociation of DnaK (Fig. 4B), the transfer efficiency

histograms of all rhodanese variants after DnaK release are reminiscent of those of the DnaJ–rhodanese complexes. Notably, even with the accelerated DnaK dissociation triggered by GrpE, refolding of rhodanese is thus not observed under our experimental conditions. Whereas substrate proteins such as luciferase have been shown to refold in the presence of the ternary chaperone system DnaJ/DnaK/GrpE under comparable conditions (49), our results suggest that for rhodanese the DnaJ–rhodanese complex is the thermodynamically most stable state. Indeed, earlier studies (13) suggested that additional chaperones, such as the chaperonin system GroEL/GroES, are required to refold denatured rhodanese. Our results therefore support the model that the DnaK/DnaJ/GrpE system passes substrate proteins on to downstream chaperones (11, 56). We note, however, that with an excess of substrate present, the cellular DnaJ and DnaK concentrations may become limiting, resulting in a less pronounced expansion or even a bypassing of the DnaK/DnaJ/GrpE system (51). Another aspect that can modulate the cellular situation is that GrpE is reversibly denatured under heat-shock conditions (57), which will increase the residence time of the individual DnaK molecules on the substrate protein and thus keep the substrate protein expanded with reduced energy consumption until the conditions are again more favorable for refolding.

In summary, we find that the binding of DnaK to rhodanese–DnaJ complexes leads to a pronounced ATP-driven expansion of the denatured substrate protein. The resulting disruption of intramolecular contacts in the substrate protein may represent an efficient way of rescuing misfolded proteins from kinetic traps that would prevent folding or could lead to aggregation. DnaK-induced protein expansion also illustrates a generic mechanism underlying the action of this versatile chaperone system: Although ATP is required for the binding of DnaK to the DnaJ–rhodanese complex, the observed expansion itself is well accounted for by an entropic effect, caused by the steric exclusion of the large DnaK molecules bound to the polypeptide chain. This “entropic pulling” (58) has been suggested to also play a dominant role in the Hsp70-mediated translocation of denatured substrate proteins into mitochondria and in protein disaggregation (59). The resulting expanded, DnaK-bound proteins are not only expected to confer solubility in the crowded cellular environment, but they also provide an ideal starting point for presenting the substrate protein to the downstream chaperone machinery.

Methods

Cysteine variants of rhodanese were expressed, purified, and labeled with Alexa Fluor 488 and Alexa Fluor 594 as described previously (60). Chaperones DnaK, DnaJ, and GrpE were gifts from H.-J. Schönfeld (Hoffmann-La Roche Ltd., Basel). All experiments were carried out in buffer A [50 mM Tris-HCl (pH 7.5), 10 mM MgCl₂, 5 mM KCl, 200 mM β-mercaptoethanol, and 0.001% (vol/vol) Tween 20 (Pierce)]. Rhodanese–chaperone complexes were formed by denaturing rhodanese in 4 M GdmCl and diluting it 100× into buffer A containing chaperones and nucleotides as indicated. Single-molecule FRET measurements were performed at 22 °C using pulsed interleaved excitation (61) on either an adapted MicroTime 200 confocal microscope (PicoQuant) or a custom-built confocal microscope. Dual-focus fluorescence correlation spectroscopy measurements were performed at 22 °C on a MicroTime 200 confocal microscope equipped with a differential interference contrast prism as described previously (29). For rapid mixing experiments, microfluidic mixers were fabricated and used as described previously (23). Molecular dynamics simulations of DnaK–rhodanese complexes were performed with CafeMol 2.0 (43) based on a Cα representation of the rhodanese chain and a structure-based model of DnaK bound to the binding sites predicted by LIMBO (44). Independent simulations of all 127 possible stoichiometry and permutations of occupied binding sites were carried out and average distance distributions and Stokes radii recovered from simulations with identical stoichiometry. For further details on experiments, instrumentation, data analysis, and simulations see [Supporting Information](#).

ACKNOWLEDGMENTS. We thank Paolo De Los Rios and Philipp Christen for helpful discussion and Hans-Joachim Schönfeld for the generous gift of chaperone proteins and expression plasmids. We thank Frank Hillger and

Daniel Streich for the design and characterization of the rhodanese variants. This work was supported by a Starting Independent Researcher grant of the

European Research Council and the Swiss National Science Foundation (to B.S. and Ambizione Grant PZ00P2_136856 to A.B.).

1. Bukau B, Weissman J, Horwich A (2006) Molecular chaperones and protein quality control. *Cell* 125(3):443–451.
2. Hartl FU, Bracher A, Hayer-Hartl M (2011) Molecular chaperones in protein folding and proteostasis. *Nature* 475(7356):324–332.
3. Mapa K, et al. (2010) The conformational dynamics of the mitochondrial Hsp70 chaperone. *Mol Cell* 38(1):89–100.
4. Schlecht R, Erbse AH, Bukau B, Mayer MP (2011) Mechanics of Hsp70 chaperones enables differential interaction with client proteins. *Nat Struct Mol Biol* 18(3):345–351.
5. Mayer MP (2010) Gymnastics of molecular chaperones. *Mol Cell* 39(3):321–331.
6. Powers ET, Powers DL, Gierasch LM (2012) FoldEco: A model for proteostasis in *E. coli*. *Cell Reports* 1(3):265–276.
7. Mayer MP, Bukau B (2005) Hsp70 chaperones: Cellular functions and molecular mechanism. *Cell Mol Life Sci* 62(6):670–684.
8. Li J, Soroka J, Buchner J (2012) The Hsp90 chaperone machinery: Conformational dynamics and regulation by co-chaperones. *Biochim Biophys Acta Mol Cell Res* 1823(3):624–635.
9. Mayer MP (2013) Hsp70 chaperone dynamics and molecular mechanism. *Trends Biochem Sci* 38(10):507–514.
10. Schröder H, Langer T, Hartl FU, Bukau B (1993) DnaK, DnaJ and GrpE form a cellular chaperone machinery capable of repairing heat-induced protein damage. *EMBO J* 12(11):4137–4144.
11. Calloni G, et al. (2012) DnaK functions as a central hub in the *E. coli* chaperone network. *Cell Reports* 1(3):251–264.
12. Diamant S, Ben-Zvi AP, Bukau B, Goloubinoff P (2000) Size-dependent disaggregation of stable protein aggregates by the DnaK chaperone machinery. *J Biol Chem* 275(28):21107–21113.
13. Langer T, et al. (1992) Successive action of DnaK, DnaJ and GroEL along the pathway of chaperone-mediated protein folding. *Nature* 356(6371):683–689.
14. Ben-Zvi A, De Los Rios P, Dietler G, Goloubinoff P (2004) Active solubilization and refolding of stable protein aggregates by cooperative unfolding action of individual hsp70 chaperones. *J Biol Chem* 279(36):37298–37303.
15. Skowrya D, Georgopoulos C, Zyliz M (1990) The *E. coli* dnaK gene product, the hsp70 homolog, can reactivate heat-inactivated RNA polymerase in an ATP hydrolysis-dependent manner. *Cell* 62(5):939–944.
16. Fenton WA, Horwich AL (2003) Chaperonin-mediated protein folding: fate of substrate polypeptide. *Q Rev Biophys* 36(2):229–256.
17. Borgia MB, et al. (2011) Single-molecule fluorescence reveals sequence-specific misfolding in multidomain proteins. *Nature* 474(7353):662–665.
18. Haran G (2012) How, when and why proteins collapse: The relation to folding. *Curr Opin Struct Biol* 22(1):14–20.
19. Hofmann H, et al. (2010) Single-molecule spectroscopy of protein folding in a chaperonin cage. *Proc Natl Acad Sci USA* 107(26):11793–11798.
20. Hillger F, et al. (2008) Probing protein-chaperone interactions with single-molecule fluorescence spectroscopy. *Angew Chem Int Ed Engl* 47(33):6184–6188.
21. Pfeil SH, Wickersham CE, Hoffmann A, Lipman EA (2009) A microfluidic mixing system for single-molecule measurements. *Rev Sci Instrum* 80(5):055105.
22. Soranno A, et al. (2012) Quantifying internal friction in unfolded and intrinsically disordered proteins with single-molecule spectroscopy. *Proc Natl Acad Sci USA* 109(44):17800–17806.
23. Wunderlich B, et al. (2013) Microfluidic mixer designed for performing single-molecule kinetics with confocal detection on timescales from milliseconds to minutes. *Nat Protoc* 8(8):1459–1474.
24. Tran HT, Mao A, Pappu RV (2008) Role of backbone-solvent interactions in determining conformational equilibria of intrinsically disordered proteins. *J Am Chem Soc* 130(23):7380–7392.
25. Mendoza JA, Rogers E, Lorimer GH, Horowitz PM (1991) Unassisted refolding of urea unfolded rhodanese. *J Biol Chem* 266(21):13587–13591.
26. Diamant S, Goloubinoff P (1998) Temperature-controlled activity of DnaK-DnaJ-GrpE chaperones: Protein-folding arrest and recovery during and after heat shock depends on the substrate protein and the GrpE concentration. *Biochemistry* 37(27):9688–9694.
27. Brinker A, et al. (2001) Dual function of protein confinement in chaperonin-assisted protein folding. *Cell* 107(2):223–233.
28. Haenni D, Zosel F, Raymond L, Nettels D, Schuler B (2013) Intramolecular distances and dynamics from the combined photon statistics of single-molecule FRET and photoinduced electron transfer. *J Phys Chem B* 117(42):13015–13028.
29. Dertinger T, et al. (2007) Two-focus fluorescence correlation spectroscopy: A new tool for accurate and absolute diffusion measurements. *ChemPhysChem* 8(3):433–443.
30. Shi YY, Hong XG, Wang CC (2005) The C-terminal (331–376) sequence of *Escherichia coli* DnaJ is essential for dimerization and chaperone activity: A small angle X-ray scattering study in solution. *J Biol Chem* 280(24):22761–22768.
31. Schuler B (2005) Single-molecule fluorescence spectroscopy of protein folding. *ChemPhysChem* 6(7):1206–1220.
32. Roder H, Colón W (1997) Kinetic role of early intermediates in protein folding. *Curr Opin Struct Biol* 7(1):15–28.
33. Pollack L, et al. (1999) Compactness of the denatured state of a fast-folding protein measured by submillisecond small-angle x-ray scattering. *Proc Natl Acad Sci USA* 96(18):10115–10117.
34. Bilsel O, Matthews CR (2006) Molecular dimensions and their distributions in early folding intermediates. *Curr Opin Struct Biol* 16(1):86–93.
35. Nettels D, Gopich IV, Hoffmann A, Schuler B (2007) Ultrafast dynamics of protein collapse from single-molecule photon statistics. *Proc Natl Acad Sci USA* 104(8):2655–2660.
36. Schuler B, Hofmann H (2013) Single-molecule spectroscopy of protein folding dynamics—expanding scope and timescales. *Curr Opin Struct Biol* 23(1):36–47.
37. Rüdiger S, Schneider-Mergener J, Bukau B (2001) Its substrate specificity characterizes the DnaJ co-chaperone as a scanning factor for the DnaK chaperone. *EMBO J* 20(5):1042–1050.
38. Mayer MP, Laufen T, Paal K, McCarty JS, Bukau B (1999) Investigation of the interaction between DnaK and DnaJ by surface plasmon resonance spectroscopy. *J Mol Biol* 289(4):1131–1144.
39. Laufen T, et al. (1999) Mechanism of regulation of hsp70 chaperones by DnaJ co-chaperones. *Proc Natl Acad Sci USA* 96(10):5452–5457.
40. Kohn JE, et al. (2004) Random-coil behavior and the dimensions of chemically unfolded proteins. *Proc Natl Acad Sci USA* 101(34):12491–12496.
41. Hofmann H, et al. (2012) Polymer scaling laws of unfolded and intrinsically disordered proteins quantified with single-molecule spectroscopy. *Proc Natl Acad Sci USA* 109(40):16155–16160.
42. Gopich IV, Szabo A (2010) FRET efficiency distributions of multistate single molecules. *J Phys Chem B* 114(46):15221–15226.
43. Kenzaki H, et al. (2011) CafeMol: A coarse-grained biomolecular simulator for simulating proteins at work. *J Chem Theory Comput* 7(6):1979–1989.
44. Van Durme J, et al. (2009) Accurate prediction of DnaK-peptide binding via homology modelling and experimental data. *PLOS Comput Biol* 5(8):e1000475.
45. Buchberger A, Valencia A, McMacken R, Sander C, Bukau B (1994) The chaperone function of DnaK requires the coupling of ATPase activity with substrate binding through residue E171. *EMBO J* 13(7):1687–1695.
46. Pierpaoli EV, et al. (1997) The power stroke of the DnaK/DnaJ/GrpE molecular chaperone system. *J Mol Biol* 269(5):757–768.
47. Theyssen H, Schuster HP, Packschies L, Bukau B, Reinstein J (1996) The second step of ATP binding to DnaK induces peptide release. *J Mol Biol* 263(5):657–670.
48. Schmid D, Baici A, Gehring H, Christen P (1994) Kinetics of molecular chaperone action. *Science* 263(5149):971–973.
49. Sharma SK, De los Rios P, Christen P, Lustig A, Goloubinoff P (2010) The kinetic parameters and energy cost of the Hsp70 chaperone as a polypeptide unfoldase. *Nat Chem Biol* 6(12):914–920.
50. Pierpaoli EV, Sandmeier E, Schönfeldt HJ, Christen P (1998) Control of the DnaK chaperone cycle by substoichiometric concentrations of the co-chaperones DnaJ and GrpE. *J Biol Chem* 273(12):6643–6649.
51. Natalello A, et al. (2013) Biophysical characterization of two different stable misfolded monomeric polypeptides that are chaperone-amenable substrates. *J Mol Biol* 425(7):1158–1171.
52. De Los Rios P, Barducci A (2014) Hsp70 chaperones are non-equilibrium machines that achieve ultra-affinity by energy consumption. *eLife (Cambridge)* 3:e02218.
53. Zyliz M, Ang D, Georgopoulos C (1987) The grpE protein of *Escherichia coli*. Purification and properties. *J Biol Chem* 262(36):17437–17442.
54. Liberek K, Marszałek J, Ang D, Georgopoulos C, Zyliz M (1991) *Escherichia coli* DnaJ and GrpE heat shock proteins jointly stimulate ATPase activity of DnaK. *Proc Natl Acad Sci USA* 88(7):2874–2878.
55. Palleros DR, Reid KL, Shi L, Welch WJ, Fink AL (1993) ATP-induced protein-Hsp70 complex dissociation requires K⁺ but not ATP hydrolysis. *Nature* 365(6447):664–666.
56. Seyffer F, et al. (2012) Hsp70 proteins bind Hsp100 regulatory M domains to activate AAA⁺ disaggregate at aggregate surfaces. *Nat Struct Mol Biol* 19(12):1347–1355.
57. Grimshaw JPA, Jelesarov I, Siegenthaler RK, Christen P (2003) Thermosensor action of GrpE. The DnaK chaperone system at heat shock temperatures. *J Biol Chem* 278(21):19048–19053.
58. De Los Rios P, Ben-Zvi A, Slutsky O, Azem A, Goloubinoff P (2006) Hsp70 chaperones accelerate protein translocation and the unfolding of stable protein aggregates by entropic pulling. *Proc Natl Acad Sci USA* 103(16):6166–6171.
59. Goloubinoff P, De Los Rios P (2007) The mechanism of Hsp70 chaperones: (Entropic) pulling the models together. *Trends Biochem Sci* 32(8):372–380.
60. Hillger F, Nettels D, Dorsch S, Schuler B (2007) Detection and analysis of protein aggregation with confocal single molecule fluorescence spectroscopy. *J Fluoresc* 17(6):759–765.
61. Müller BK, Zaychikov E, Bräuchle C, Lamb DC (2005) Pulsed interleaved excitation. *Biophys J* 89(5):3508–3522.

Supporting Information

Kellner et al. 10.1073/pnas.1407086111

SI Methods

Sample Preparation. One single-cysteine variant (rhodanese K174C) and five different double-cysteine variants of rhodanese ($\Delta 39$ K135C/K174C, $\Delta 49$ K236C/E285C, $\Delta 58$ E77C/K135C, $\Delta 117$ D102C/D219C, and $\Delta 159$ E77C/K236C) were produced by site-directed mutagenesis. The rhodanese variants were prepared as previously described for wild-type rhodanese (1). All five double-cysteine rhodanese variants were labeled with Alexa Fluor 488 and Alexa Fluor 594 as described before (2), whereas rhodanese K174C was labeled with Alexa Fluor 488 C5 maleimide (Invitrogen, Molecular Probes) according to the manufacturer's instructions using maleimide-thiol chemistry. Briefly, a twofold molar excess of Alexa Fluor 488 and Alexa Fluor 594 maleimide derivatives was added to the protein. After 1 h of incubation at room temperature, unreacted dye was removed by gel filtration. Variants $\Delta 39$ and $\Delta 117$ contained a large fraction of doubly labeled Alexa 488-labeled molecules. A large part of this incorrectly labeled species was removed by anion exchange chromatography, which was performed on an ÄKTA purifier FPLC system with a MonoQ 5/50 GL column (GE Healthcare). For the $\Delta 117$ variant, the system was equilibrated in 10 mM Tris-HCl buffer, pH 8.5, and eluted with a gradient from 0 to 200 mM sodium chloride over 60 mL (12 column volumes). The $\Delta 39$ variant was purified in 50 mM Tris-HCl, pH 7.0, and eluted with a gradient from 0 to 500 mM sodium chloride over 60 mL (12 column volumes). To test the structural integrity of the fluorophore-labeled rhodanese variants, their enzymatic activity was determined as described by Westley (3). The labeled rhodanese variants exhibited an activity similar to wild-type rhodanese (wild-type: $0.9 \text{ mmol min}^{-1} \text{ mg}^{-1}$, $\Delta 39$: $1.0 \text{ mmol min}^{-1} \text{ mg}^{-1}$, $\Delta 49$: $0.5 \text{ mmol min}^{-1} \text{ mg}^{-1}$, $\Delta 58$: $0.6 \text{ mmol min}^{-1} \text{ mg}^{-1}$, and $\Delta 117$: $0.6 \text{ mmol min}^{-1} \text{ mg}^{-1}$). DnaK, DnaJ, and GrpE were gifts from H.-J. Schönfeld (Hoffmann-La Roche Ltd., Basel). The concentrations of the stock solutions were 100 μM for DnaK and DnaJ and 200 μM for GrpE in 50 mM Tris-HCl, pH 7.7, and 100 mM NaCl.

To form rhodanese-chaperone complexes, rhodanese was denatured in 4 M guanidinium chloride (GdmCl) in buffer A (50 mM Tris-HCl, 10 mM MgCl_2 , 5 mM KCl, 200 mM β -mercaptoethanol, and 0.001% Tween 20) and refolded by 100 \times dilution into buffer A in the absence of GdmCl and in the presence of DnaK, DnaJ, GrpE, and nucleotides at the indicated concentrations directly before the measurements. The final rhodanese concentration was between 25 and 75 pM. Native rhodanese was measured in buffer A; denatured rhodanese under native conditions was measured in the microfluidic mixing device described below.

Single-Molecule Fluorescence Spectroscopy. Single-molecule FRET (smFRET) measurements were performed at 22 $^\circ\text{C}$ using either a MicroTime 200 confocal microscope (PicoQuant) or a custom-built confocal microscope. Both instruments use pulsed interleaved excitation (4). Pulses for acceptor excitation were generated by a SC450-PP super continuum fiber laser (Fianium) operating at a 20-MHz repetition rate. The wavelength was selected with a z582/15 band-pass filter (Chroma Technology), and the power, measured at the back aperture of the microscope objective, was set to 35 μW ; 483-nm donor excitation pulses (100 μW at the back aperture) were obtained from an LDH-D-C-485 diode laser (PicoQuant). The driving electronics of the diode laser (Sepia II; PicoQuant) were triggered by infrared light of the Fianium laser detected on a fast photodiode (DET10a/M; Thorlabs). The lasers were focused into the sample solutions with a UPlanApo 60 \times /1.20W objective (Olympus). The fluorescence

signal passed a chromatic beam splitter (R405/488/594 or z488/568; Chroma Technology) and a 100- μm pinhole before further distribution according to polarization (polarizing beam splitter cube) and wavelength (dichroic mirrors 595 DCXR or 585 DCXR; Chroma Technology) onto four detection channels equipped with avalanche photodiodes. Before detection, the emission was finally filtered by ET525/50M or HQ650/100 band-pass filters (Chroma Technology) for donor and acceptor fluorescence, respectively. Time-correlated single-photon counting electronics (HydraHarp 400; PicoQuant) recorded each photon detection pulse with 16-ps time resolution.

The brightness of the rhodanese-chaperone complexes was determined by measuring the fluorescence emission of ~ 2 nM singly labeled rhodanese K174C-Alexa 488 alone or in complex with DnaJ (0.5 μM DnaJ) or DnaK (10 μM DnaK, 0.5 μM DnaJ, and 1 mM ATP) on the confocal microscope. The fluorophore was excited at 485 nm with 100 μW at 40 MHz with the diode laser, and only one detector was used.

Data Reduction. Only photons detected after donor excitation pulses were used for construction of FRET efficiency histograms, whereas photons after acceptor excitation pulses were used to probe whether a molecule carried an active acceptor fluorophore. Successive photons with interphoton times of less than 150 μs detected in any channel following donor excitation pulses were combined into one photon burst. Only bursts containing more than 35 photons after correction for background, differences in quantum yields of the fluorophores, different collection efficiencies of the detection channels, cross-talk, and direct excitation of the acceptor (5) were used for further analysis. Bursts with a significant likelihood for acceptor photobleaching were excluded from further analysis as described previously (6). Transfer efficiencies were calculated for each burst from $E = n_A/(n_D + n_A)$, where n_D and n_A are the corrected donor and acceptor counts detected after donor excitation, respectively (5). Bursts were further analyzed for the stoichiometry ratio (7), $S = n_{Dexc}/(n_{Dexc} + n_{Aexc})$, where n_{Dexc} is the total number of counts after the donor excitation and n_{Aexc} is the total number of counts after acceptor excitation. Molecules lacking an active acceptor dye yield a stoichiometry ratio close to 1 and were excluded from FRET efficiency histograms. Histograms were constructed with a bin width of 0.03.

To quantify the kinetics of conformational changes on the timescale of minutes and longer, moving window analysis was used (8). We constructed series of FRET efficiency histograms from long single-molecule measurements (0.5–2 h) by splitting them into overlapping intervals of 5-min duration starting every 100 s. FRET efficiency histograms obtained from the bursts of each interval were constructed and represented as lines in time-resolved FRET efficiency histograms (FRET kinetics) in which the color indicates the time, increasing from blue to green.

Donor fluorescence anisotropies were determined from photons arriving at the donor detectors after 485-nm excitation and acceptor anisotropies from photons arriving at the acceptor detectors after 590-nm acceptor direct excitation. The G-factor of the instrument (a correction for different detection efficiencies for parallel and perpendicular polarized light) was calibrated to be 1.245 by comparison of ensemble fluorescence anisotropy measurements with measurements at the confocal smFRET setup of free dye in water and 50% glycerol. To account for the optical path and the high-numerical-aperture objective in the confocal setup, additional correction factors were determined according to Koshioka et al. (9). We found the correction factors to be $L_1 = 0.098$

and $L_2 = 0.094$ for 485-nm excitation and $L_1 = 0.111$ and $L_2 = 0.058$ for 590-nm excitation. Anisotropies were calculated as

$$r = \frac{I_{\parallel} - G I_{\perp}}{(1 - 3 L_2) I_{\parallel} + (2 - 3 L_1) G I_{\perp}}, \quad [\text{S1}]$$

where I_{\parallel} and I_{\perp} denote the fluorescence intensity for parallel and perpendicular polarized light with respect to the polarization of the excitation light, respectively (Table S2).

Microfluidic Mixing. For probing kinetics on timescales shorter than minutes, we used the microfluidic mixing device described in detail by Wunderlich et al. (10). To observe the association of DnaK with DnaJ–rhodanese complexes, DnaJ–rhodanese $\Delta 39$ complexes were preformed as described above with a final concentration of 0.55 μM DnaJ and with 22 μM ATP. This solution was supplied to the side channels of the microfluidic device and mixed with 100 μM DnaK (50 mM Tris-HCl, pH 7.7, and 100 mM NaCl) present in the central channel. The mixer was operated at a flow velocity of 1 mm/s (fully developed flow in the observation channel) and at a mixing ratio of 1:9 to obtain final concentrations in the observation channel of 10 μM DnaK, 20 μM ATP, and 0.5 μM DnaJ. These conditions were obtained by applying 15.1 kPa (2.19 psi) and 16.1 kPa (2.33 psi) at the main and side inlet channels, respectively. The concentration of Tween 20 in buffer A was increased to 0.01% to prevent nonspecific interactions of the chaperone–substrate complexes with the polydimethylsiloxane surfaces of the microfluidic mixing channels. The confocal volume was focused into the observation channel at different positions downstream from the mixing region, corresponding to different times after mixing. Fluorescence bursts were detected at each position for 30 min. Positions were converted to times after mixing as described by Wunderlich et al. (11). Histograms were obtained for 1, 5, 7.5, 10, 20, 30, 40, and 50 s after mixing.

Transfer efficiency histograms of denatured rhodanese under native conditions (buffer A with 0.4 M GdmCl) were obtained by mixing denatured rhodanese in 4 M GdmCl (central channel) with buffer A (side channels) at an average flow rate of 0.8 mm/s in the observation channel and placing the confocal volume at a position 100 μm (125 ms) downstream of the mixing region. The applied pressures were 10.4 kPa (1.5 psi) in the side channels and 6.8 kPa (1 psi) in the central channel.

For combining manual and microfluidic mixing smFRET experiments (Fig. 3) the transfer efficiency histograms were normalized by the total number of bursts. Fractions of bursts with transfer efficiencies from 0.0 to 0.3 and 0.6 to 0.8 were used for monitoring the progress of the DnaK complex and DnaJ complex interconversion. The two curves were fitted globally to double exponential decays with common rate constants, yielding $k_1 = 0.028 \text{ s}^{-1}$ and $k_2 = 0.002 \text{ s}^{-1}$.

Dual-Focus Fluorescence Correlation Spectroscopy. Dual-focus fluorescence correlation spectroscopy (2f-FCS) measurements were performed at 22 °C on a MicroTime 200 confocal microscope equipped with a Nomarski prism (12). Two orthogonally polarized diode lasers at 483 nm (LDH-D-C-485; PicoQuant) with repetition rates of 20 MHz and laser powers of 30 μW (at the back aperture of the microscope objective) each were used to excite the sample alternately. The emission light passed through a 150- μm pinhole and was focused onto the detectors (tau-SPAD50; PicoQuant). The distance between the two foci was measured to be $440 \pm 10 \text{ nm}$ as described previously (13). All 2f-FCS experiments were performed with rhodanese K174C Alexa 488 at a final concentration of 0.5 nM. The auto- and cross-correlation functions of both foci were analyzed globally as described by Dertinger et al. (12), and the resulting translational diffusion coefficients, D , were converted into Stokes

radii (R_S) using the Stokes–Einstein equation (14), where k_B is the Boltzmann constant, T the temperature, and η the solvent viscosity:

$$R_S = \frac{k_B T}{6 \pi \eta D}. \quad [\text{S2}]$$

Bimolecular Association Rate of DnaJ and Denatured Rhodanese. Assuming that unfolded rhodanese will partition to its native conformation or bind to DnaJ as shown in Fig. S1A, we estimated the bimolecular association rate coefficient, $k_{on, DnaJ}$, for the DnaJ–rhodanese complex from the fraction of native rhodanese, f_N , after dilution of unfolded protein in the presence of DnaJ according to

$$k_{on, DnaJ} = \frac{1 - f_N}{f_N} k_{fold} [DnaJ]. \quad [\text{S3}]$$

The folding rate constants, k_{fold} , of the variants were determined from independent kinetic measurements where unfolded rhodanese was diluted into native buffer in the absence of chaperones (Fig. S1C). A single-exponential rise was fitted to the change of the number of bursts within the transfer efficiency range corresponding to the native subpopulations (Fig. S1F and Table S1). f_N was estimated from smFRET measurements of rhodanese after dilution into native buffer in the absence (Fig. S1D) and presence (Fig. S1E) of 0.5 μM DnaJ. The data in Fig. S1D were fitted with a Gaussian. Subsequently, the data in Fig. S1E were fitted with Gaussians with identical positions and widths. The values of f_N were estimated from a comparison of the amplitudes of the fitted Gaussians (Table S1).

Estimation of the Stoichiometry of DnaJ–Rhodanese Complexes. The R_S of rhodanese and DnaJ–rhodanese complexes formed at 0.5 μM DnaJ were determined from five independent 2f-FCS measurements. Assuming a spherical shape, the molecular weight (MW) of a complex was estimated (Eq. S4) from R_S , where we used the average molar mass of amino acids $m_{aa} = 111 \text{ g/mol}$ (weighted for their abundance in proteins) (15) and the average Stokes volume of an amino acid $v_{aa} = 0.27 \text{ nm}^3$ (Table S3) (13, 16):

$$MW = \rho V_S = \frac{m_{aa}}{v_{aa}} \frac{4 \pi}{3} R_S^3. \quad [\text{S4}]$$

v_{aa} was determined as follows. For a compact chain with a spherical shape, the radius of gyration, R_G , and the R_S are related by

$$R_G = \sqrt{\frac{3}{5}} R_S. \quad [\text{S5}]$$

R_G and R_S scale with the number of amino acid residues N according to

$$R_G = a N^{\frac{1}{3}} \quad [\text{S6}]$$

and

$$R_S = b N^{\frac{1}{3}}. \quad [\text{S7}]$$

Dima and Thirumalai (16) determined $a = 0.3 \text{ nm}$ from ~ 400 PDB structures of monomeric globular proteins, thus $b = 0.4 \text{ nm}$. This value is in good agreement with $b = 0.47 \text{ nm}$ obtained by Wilkins et al. (17). Finally, v_{aa} is given by

$$v_{aa} = \frac{4 \pi}{3} b^3. \quad [\text{S8}]$$

Molecular Dynamics Simulations of Rhodanese Bound to Different Numbers of DnaK Molecules. Protein structures were simplified using one bead per amino acid corresponding to the position of the C α atom. Unfolded rhodanese was modeled using a flexible local potential (AICG2 in CafeMol) dependent on the amino acid sequence that was shown to reasonably reproduce the conformational distribution of unfolded states or intrinsically disordered proteins (18). An additional potential term, accounting for intrachain hydrophobic interactions, was added to better reproduce the compact unfolded state of rhodanese under native conditions. This multibody potential term (HP in CafeMol) depends on the surface exposure of each amino acid (19) and its weight was tuned to obtain a radius of gyration for unfolded rhodanese close to what was determined by smFRET experiments.

DnaK was modeled with a structure-based model (20) using the NMR structure of *Escherichia coli* DnaK complexed with ADP and substrate (PDB ID code 2KHO) as a reference conformation. Nonbonded native interactions involving residues in the flexible interdomain linker were switched off and the AICG2 potential was used to model this region. Using this setup, it was possible to limit the conformational flexibility of the individual domains while allowing significant fluctuations of the interdomain arrangement in agreement with NMR residual dipolar coupling analysis (21).

To model DnaK–rhodanese complexes, the substrate peptide present in the NMR structure of ADP-bound DnaK was replaced by the corresponding part of an extended rhodanese chain. Artificial harmonic restraints were imposed on the interresidue distances between the rhodanese chain and DnaK binding residues to preserve the binding arrangement. Apart from these restraints, the interactions between rhodanese and DnaK molecules were limited to excluded volume effects.

Seven potential DnaK binding sites were identified in the rhodanese sequence according to the predictor proposed by Van Durme et al. (22). [Another algorithm by Rüdiger et al. (23) yielded similar binding sites; Fig. S4.] This resulted in seven possible stoichiometries (rhodanese:DnaK_{*n*} with *n* = 1–7) and a total of (2⁷ – 1) = 127 possible distinct molecular complexes. Each individual complex was simulated using Langevin dynamics with a temperature *T* = 300 K for ~108 time steps with an integration step size of 0.1 *t*, where *t* corresponds to CafeMol time units (*t* ~200 fs) (24). Only the configurations corresponding to the second half of each trajectory were used to calculate the distance distributions reported in Fig. 2.

R_G and end-to-end distance distributions for the simulated rhodanese–DnaK_{*n*} complexes were calculated from the simulation results and are represented in Table S4. Distance distributions for polypeptide chain segments on the rhodanese chain corresponding to the label positions of the rhodanese variants used in smFRET experiments were extracted and converted to transfer efficiencies with

$$\langle E \rangle_{simulation} = \sum P(r) E(r) dr. \quad [\text{S9}]$$

Stokes radii were estimated from simulation snapshots with HydroPro (25) calculations based on a bead model where each residue corresponded to an element with a *R_S* equal to 6.1 Å. The harmonic average of the results corresponding to each stoichiometry was then used for estimating the mean *R_S* reported in Table S4.

Mean Transfer Efficiency, Mean Interdye Distance, End-To-End Distances, and Radii of Gyration of DnaK–Rhodanese Complexes from smFRET Histograms. Analyzing the FRET efficiency histograms of rhodanese–DnaK complexes in terms of quantitative distance distributions is complicated by the static and dynamic heterogeneity of the system. The broadening beyond shot noise indicates interconversion between different conformations or rhodanese/DnaK stoichiometries on the millisecond timescale

and/or above, but faster reconfiguration dynamics are likely to be present also. Note, however, that the average transfer efficiencies of the subpopulations corresponding to the rhodanese–DnaK complexes are independent of these dynamics as long as they interconvert slowly on the fluorescence lifetime of the dyes (26), which is a reasonable assumption because this applies even to unfolded and intrinsically disordered proteins in the absence of bound chaperones (27, 28). Given the only moderately high anisotropies of the fluorophores (Table S2), a pronounced effect of the orientational distribution on the transfer efficiencies is unlikely (29).

We therefore use the following procedure. The mean transfer efficiencies of the DnaK–rhodanese complexes were determined from the histograms of rhodanese in the presence of 10 μM DnaK, 0.5 μM DnaJ, and 1 mM ATP (Fig. 1E). To account for the residual population of rhodanese molecules that are not bound by DnaK but are either folded or bound to DnaJ, the histograms were fitted to the sum of a log-normal function, *P*(*E*), and an interpolation function obtained from the histograms in the presence of DnaJ (Fig. 1D). The mean transfer efficiencies, $\langle E \rangle$, of the DnaK–rhodanese complexes were then calculated from

$$\langle E \rangle = \frac{\int_{-0.2}^{1.2} P(E) E dE}{\int_{-0.2}^{1.2} P(E) dE} \quad [\text{S10}]$$

and converted to root mean square interdye distances, $\langle r^2 \rangle^{1/2}$, by numerically solving Eq. S11:

$$\langle E \rangle = \frac{\int P(r) E(r) dr}{\int P(r) dr}. \quad [\text{S11}]$$

We assume normal distributions for *P*(*r*) (Eq. S12) because they provide a good approximation of the distance distributions observed in the simulations of the rhodanese–DnaK complexes (Fig. 2B):

$$P(r) = \frac{1}{\sqrt{2\pi} \sigma^2} e^{-\frac{(r-r)^2}{2\sigma^2}}. \quad [\text{S12}]$$

The lowest overall mean square deviation between the average transfer efficiencies of all rhodanese variants obtained from the smFRET experiments and the simulations is observed for six DnaK molecules bound (*N_{DnaK}* = 6) (Fig. 2C). The values of σ in Eq. S12 were thus taken from the fits of normal distributions to the interdye distance distributions obtained from the molecular dynamics (MD) simulations of six DnaK (*N_{DnaK}*) molecules bound to rhodanese. The distance dependence of the transfer efficiency is given by the Förster equation (Eq. S13) with the Förster radius *R₀* = 5.4 nm for Alexa 488 and Alexa 594 (30):

$$E(r) = \frac{1}{1 + (r/R_0)^6}. \quad [\text{S13}]$$

To estimate, from the intramolecular distance distributions of the different rhodanese variants determined in this way, the average end-to-end distance of rhodanese in complex with DnaK, we use the scaling of the average intramolecular distance with the sequence separation of the labeling positions obtained from the simulations. First, the average interdye distance, $\langle r \rangle$, as a function of the amino acid sequence separation between the label positions, Δaa , from the MD simulations of the different numbers of DnaK molecules bound to rhodanese was fit to

$$\langle r \rangle (\Delta aa) = g \Delta aa^x. \quad [\text{S14}]$$

For *N_{DnaK}* = 6, a scaling exponent of *x* = 0.71 was obtained. Eq. S14 with *x* = 0.71 was then used to fit the interdye distances from the experimental data as function of the sequence separation and

extrapolated to the average end-to-end distance, $\langle r_{ee} \rangle$, of rhodanese in complex with DnaK, yielding $\langle r_{ee} \rangle = 17.3 \pm 0.3$ nm. The uncertainty of the extrapolation was estimated by varying x in the range obtained for $N_{DnaK} = 5$ to $N_{DnaK} = 7$. Finally, we used the average ratio $R_G/\langle r_{ee} \rangle$ calculated from the simulations for $N_{DnaK} = 5$ to $N_{DnaK} = 7$, 2.4 ± 0.1 , to convert the experimental value of $\langle r_{ee} \rangle$ to $R_G = 7.2 \pm 0.3$ nm (Table S4).

Dissociation of the DnaK–Rhodanese Complex at Single-Turnover ATP Concentrations. To determine the dissociation rate constant of DnaK and rhodanese, DnaK–rhodanese complexes were formed

at 0.5 μ M DnaJ, 10 μ M DnaK, and 10 μ M ATP (i.e., equimolar concentrations of DnaK and ATP). The subsequent dissociation of the complex was observed by smFRET measurements for 30 min (Fig. 4B). The total numbers of bursts observed per time interval were determined for all variants (Fig. 4C), and the resulting decays in burst numbers were fitted with a single-exponential function. The mean of the five rate constants obtained (Table S1) is $k_{diss, DnaK} = (2.5 \pm 0.4) 10^{-3} \text{ s}^{-1}$. The kinetics of the change in R_S determined from 2f-FCS measurements (Fig. 4A) yielded $k_{diss, DnaK} = (1.7 \pm 0.4) 10^{-3} \text{ s}^{-1}$.

- Miller DM, et al. (1992) Recombinant bovine rhodanese: Purification and comparison with bovine liver rhodanese. *Biochim Biophys Acta* 1121(3):286–292.
- Hillger F, Nettels D, Dorsch S, Schuler B (2007) Detection and analysis of protein aggregation with confocal single molecule fluorescence spectroscopy. *J Fluoresc* 17(6):759–765.
- Westley J (1981) Thiosulfate: Cyanide sulfurtransferase (rhodanese). *Methods Enzymol* 77:285–291.
- Müller BK, Zaychikov E, Bräuchle C, Lamb DC (2005) Pulsed interleaved excitation. *Biophys J* 89(5):3508–3522.
- Schuler B (2007) Application of single molecule Förster resonance energy transfer to protein folding. *Methods Mol Biol* 350:115–138.
- Kudryavtsev V, et al. (2012) Combining MFD and PIE for accurate single-pair Förster resonance energy transfer measurements. *ChemPhysChem* 13(4):1060–1078.
- Kapanidis AN, et al. (2004) Fluorescence-aided molecule sorting: Analysis of structure and interactions by alternating-laser excitation of single molecules. *Proc Natl Acad Sci USA* 101(24):8936–8941.
- Hofmann H, et al. (2010) Single-molecule spectroscopy of protein folding in a chaperonin cage. *Proc Natl Acad Sci USA* 107(26):11793–11798.
- Koshioka M, Sasaki K, Masuhara H (1995) Time-dependent fluorescence depolarization analysis in 3-dimensional microspectroscopy. *Appl. Spect.* 49(2):224–228.
- Wunderlich B, et al. (2013) Microfluidic mixer designed for performing single-molecule kinetics with confocal detection on timescales from milliseconds to minutes. *Nat Protoc* 8(8):1459–1474.
- Wunderlich B, Nettels D, Schuler B (2014) Taylor dispersion and the position-to-time conversion in microfluidic mixing devices. *Lab Chip* 14(1):219–228.
- Dertinger T, et al. (2007) Two-focus fluorescence correlation spectroscopy: A new tool for accurate and absolute diffusion measurements. *ChemPhysChem* 8(3):433–443.
- Hofmann H, et al. (2012) Polymer scaling laws of unfolded and intrinsically disordered proteins quantified with single-molecule spectroscopy. *Proc Natl Acad Sci USA* 109(40):16155–16160.
- Einstein A (1905) The motion of elements suspended in static liquids as claimed in the molecular kinetic theory of heat. *Ann Phys-Berlin* 17(8):549–560.
- Jordan IK, et al. (2005) A universal trend of amino acid gain and loss in protein evolution. *Nature* 433(7026):633–638.
- Dima RI, Thirumalai D (2004) Asymmetry in the shapes of folded and denatured states of proteins. *J Phys Chem B* 108(21):6564–6570.
- Wilkins DK, et al. (1999) Hydrodynamic radii of native and denatured proteins measured by pulse field gradient NMR techniques. *Biochemistry* 38(50):16424–16431.
- Terakawa T, Takada S (2011) Multiscale ensemble modeling of intrinsically disordered proteins: p53 N-terminal domain. *Biophys J* 101(6):1450–1458.
- Fujitsuka Y, Takada S, Luthey-Schulten ZA, Wolynes PG (2004) Optimizing physical energy functions for protein folding. *Proteins* 54(1):88–103.
- Clementi C, Nymeyer H, Onuchic JN (2000) Topological and energetic factors: What determines the structural details of the transition state ensemble and “en-route” intermediates for protein folding? An investigation for small globular proteins. *J Mol Biol* 298(5):937–953.
- Bertelsen EB, Chang L, Gestwicki JE, Zuiderweg ERP (2009) Solution conformation of wild-type E. coli Hsp70 (DnaK) chaperone complexed with ADP and substrate. *Proc Natl Acad Sci USA* 106(21):8471–8476.
- Van Durme J, et al. (2009) Accurate prediction of DnaK-peptide binding via homology modelling and experimental data. *PLoS Comput Biol* 5(8):e1000475.
- Rüdiger S, Germeroth L, Schneider-Mergener J, Bukau B (1997) Substrate specificity of the DnaK chaperone determined by screening cellulose-bound peptide libraries. *EMBO J* 16(7):1501–1507.
- Kenzaki H, et al. (2011) CafeMol: A coarse-grained biomolecular simulator for simulating proteins at work. *J Chem Theory Comput* 7(6):1979–1989.
- Ortega A, Amorós D, García de la Torre J (2011) Prediction of hydrodynamic and other solution properties of rigid proteins from atomic- and residue-level models. *Biophys J* 101(4):892–898.
- Schuler B, Lipman EA, Steinbach PJ, Kumke M, Eaton WA (2005) Polyproline and the “spectroscopic ruler” revisited with single-molecule fluorescence. *Proc Natl Acad Sci USA* 102(8):2754–2759.
- Soranno A, et al. (2012) Quantifying internal friction in unfolded and intrinsically disordered proteins with single-molecule spectroscopy. *Proc Natl Acad Sci USA* 109(44):17800–17806.
- Nettels D, Gopich IV, Hoffmann A, Schuler B (2007) Ultrafast dynamics of protein collapse from single-molecule photon statistics. *Proc Natl Acad Sci USA* 104(8):2655–2660.
- Hillger F, et al. (2008) Probing protein-chaperone interactions with single-molecule fluorescence spectroscopy. *Angew Chem Int Ed Engl* 47(33):6184–6188.
- Schuler B, Lipman EA, Eaton WA (2002) Probing the free-energy surface for protein folding with single-molecule fluorescence spectroscopy. *Nature* 419(6908):743–747.

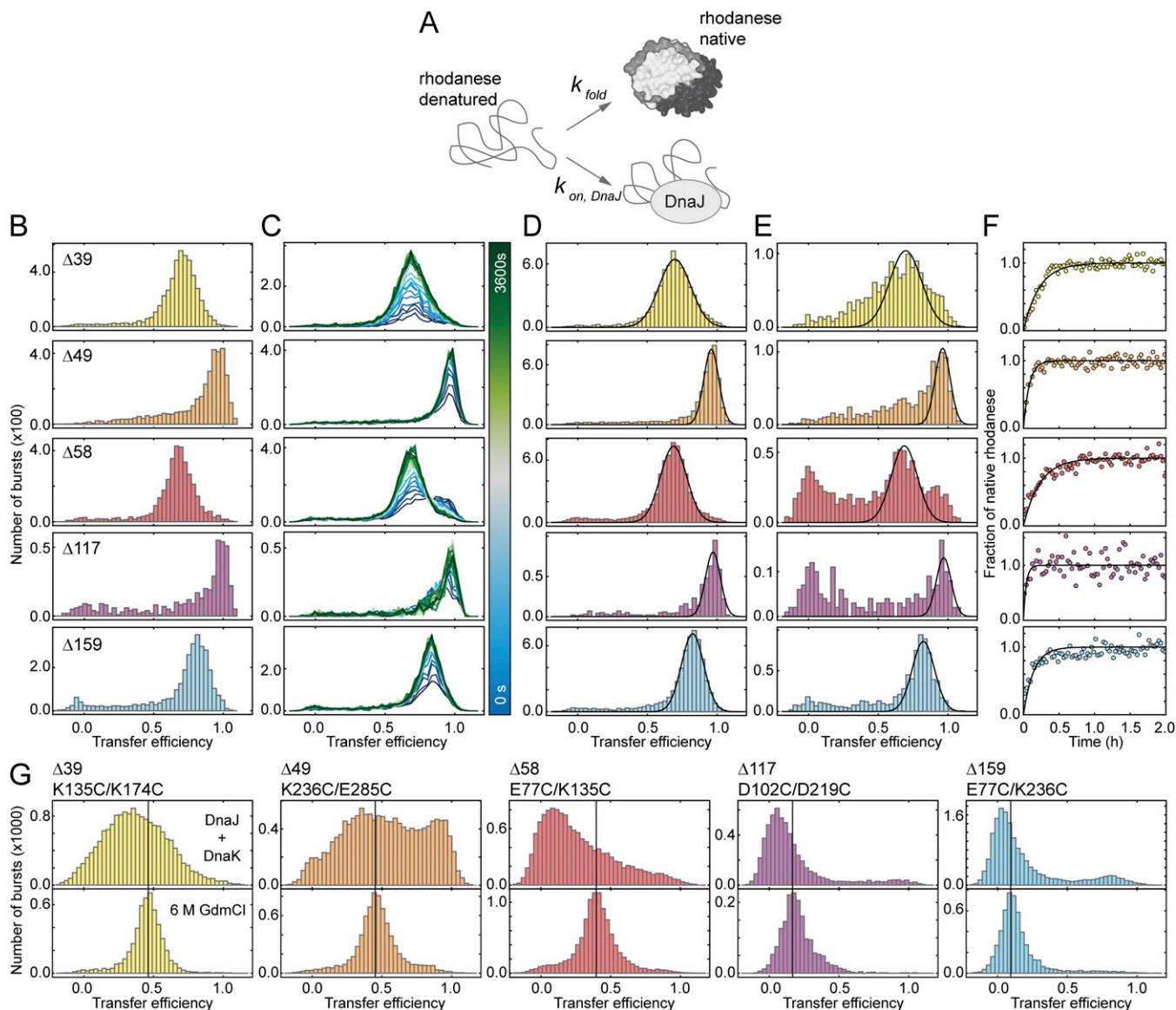


Fig. S1. Refolding of rhodanese in the absence and presence of the co-chaperone DnaJ for estimation of the bimolecular association rate coefficient for the formation of DnaJ–rhodanese complexes. (A) Kinetic model used for the determination of $k_{on, DnaJ}$. (B) Transfer efficiency histograms of native rhodanese variants. Each histogram was recorded for 5 min. (C) FRET kinetics of refolding rhodanese (1 h of measurement time is shown). (D) Transfer efficiency histograms of native rhodanese after complete refolding in absence of chaperones. Histograms are constructed from the last 10 min of the 2-h measurements presented in C. The native populations were fitted with Gaussian peaks (black lines). (E) Transfer efficiency histograms of rhodanese after refolding in the presence of $0.5 \mu\text{M}$ DnaJ. Histograms are constructed from 10-min measurements recorded 50 min after dilution into native buffer. Gaussian peaks with the same positions and widths as in C were used to estimate the native-state subpopulations (black lines). The small populations at zero transfer efficiency in E (note the axis scaling and the small amplitudes of this population compared with D) originate from incomplete elimination of molecules with inactive acceptor fluorophores by pulsed interleaved excitation. (F) Refolding of rhodanese under single-molecule conditions observed as an increase in the fraction of native protein from data in C. Black lines indicate single exponential fits. (G) Comparison of the transfer efficiency histograms of rhodanese in the presence of 6 M GdmCl (Lower) and in complex with $10 \mu\text{M}$ DnaK (in the presence of $0.5 \mu\text{M}$ DnaJ, 1 mM ATP; Upper). The black vertical lines indicate the transfer efficiency maxima of the rhodanese variants denatured in 6 M GdmCl.

1 **VHQVLYRALV S**TRKWLAE^{ABC}SVR AGKVG**PGLRV** LDASWYSPGT REARKEYLER
 51 HVPGASFFDI EECRDKASPY EVMLPSEAGF ADYVGLGIS NDTHVVYDGG
 101 DDLGSFYAPR V**MMFRVFGH** RT**VSVLNGGF** RNWIK**EGHPV** TSEPSRPEPA
 151 IFKATL**NRS**L **LKTYE**QVLEN LESKR**FQLVD** SRAQ**CRYLGT** Q**PE**PDVAVGLD
 201 SGHIRGSVNM PFMNFLTEDG FEKSPEELRA MFEAKKVDLT K**PLIATCR**KG
 251 VTACH**IALAA** **YLC**GKPDVAI YDGS**NFEWFH** R**APP**ETWVSQ GKGKGA

ABC DnaK-binding sites predicted by Van Durme *et al.*

ABC DnaK-binding sites predicted by Rüdiger *et al.*

Fig. 54. DnaK binding sites in the rhodanese amino acid sequence. DnaK binding sites were predicted with the LIMBO algorithm by van Durme *et al.* (22) (red) and with the algorithm of Rüdiger *et al.* (23) (bold).

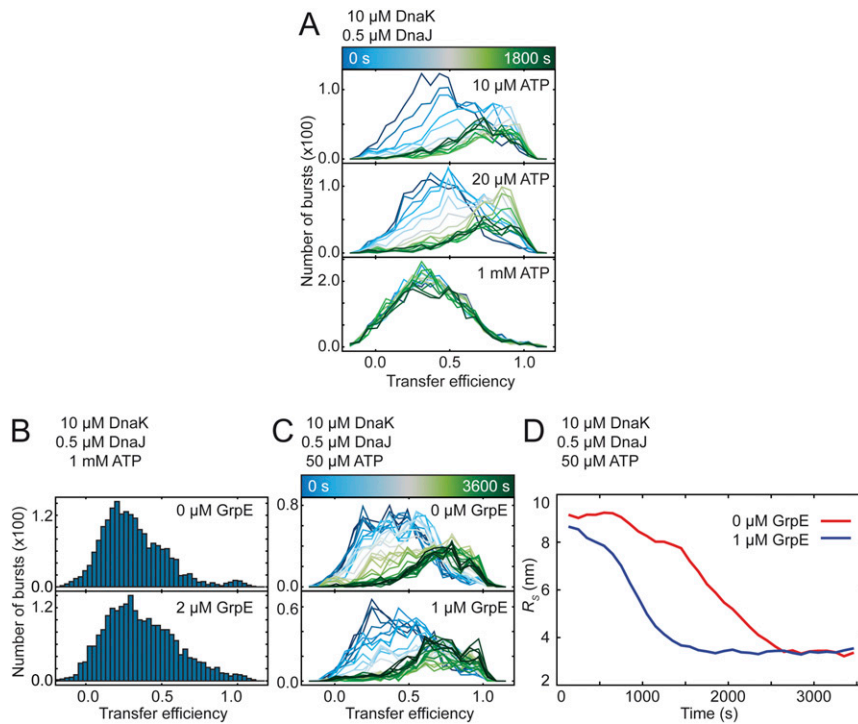


Fig. 55. The concentrations of ATP and GrpE modulate the kinetic stability of rhodanese–DnaK complexes. (A) FRET kinetics (30 min) of rhodanese ($\Delta 39$) in the presence of 0.5 μM DnaJ, 10 μM DnaK, and ATP at indicated concentrations. (B) Transfer efficiency histograms of rhodanese in the presence of 10 μM DnaK, 0.5 μM DnaJ, and 1 mM ATP in the absence and presence of 2 μM GrpE, measured for 30 min. (C) FRET kinetics (1 h) of rhodanese ($\Delta 39$) in the presence of 0.5 μM DnaJ, 10 μM DnaK, 50 μM ATP, and GrpE as indicated. (D) Changes in R_2 determined from 2f-FCS measured under the same conditions as in C.

Table S2. Steady-state anisotropies of Alexa 488 and Alexa 594 and brightness of Alexa 488 bound to rhodanese ($\Delta 39$ or rhodanese K174C Alexa 488) in complex with DnaJ (0.5 μM DnaJ) or DnaK (0.5 μM DnaJ, 10 μM DnaK, and 1 mM ATP) or native without chaperones

Molecular species	Anisotropy Alexa 488	Anisotropy Alexa 594	Brightness, cps
Native rhodanese	0.15	0.24	8.9×10^4
DnaJ–rhodanese complex	0.22	0.28	1.3×10^4
DnaK–rhodanese complex	0.21	0.25	5.6×10^4

Table S3. Comparison of theoretical and experimental Stokes radii, R_S , and molecular masses of DnaJ–rhodanese complexes (DnaJ molecules counted as monomers) of different stoichiometries estimated from Eq. S4

Theoretical values	Rhodanese	Rhodanese + 1 DnaJ	Rhodanese + 2 DnaJ	Rhodanese + 3 DnaJ	Rhodanese + 4 DnaJ
Molecular mass (kD)	33	74	115	156	197
Stokes Radius R_S (nm) from Eq. S4	2.7	3.5	4.1	4.5	4.9
Experimental values (2f-FCS)	Rhodanese		DnaJ – rhodanese complex		
Measured R_S (nm)	2.6 ± 0.1		3.1 ± 0.2		
Molecular mass (kD) from Eq. S4	30		51		

Table S4. Stokes radii, R_S , (HydroPro) (25), average end-to-end distances, $\langle r_{ee} \rangle$, and radii of gyration, R_G , for rhodanese in complex with different numbers of DnaK molecules from MD simulations and estimation of R_G for single-molecule FRET experiments based on the shape of the distance distributions from the MD simulations

N_{DnaK}	$\langle r_{ee} \rangle$ simulation, nm	R_G simulation, nm	$\langle r_{ee} \rangle / R_G$ simulation	R_G experiment, nm	R_S simulation, nm
0					3.6
1					5.2
2					6.3
3					7.2
4					8.0
5	21.0	9.2	2.3	7.5	8.8
6	23.3	9.6	2.4	7.2	9.5
7	24.8	10.0	2.5	6.9	9.9
Mean			2.4 ± 0.1	7.2 ± 0.3	